

Research Article

Open Access



Integrated control of anti-lock and regenerative braking for in-wheel-motor-driven electric vehicles

Jiawang Yong¹, Yiyao Dong¹, Zhilin Zhang², Nenglian Feng³, Wanting Li¹

¹Department of Traffic Engineering, Beijing University of Technology, Beijing 100124, China.

²Hefei SEEKTOP Automotive Technology Co., Ltd, Hefei 230601, Anhui, China.

³Faculty of Environment and Life, Beijing University of Technology, Beijing 100124, China.

Correspondence to: Dr. Jiawang Yong, Department of Traffic Engineering, Beijing University of Technology, No. 100 Pingleyuan, Chaoyang District, Beijing 100124, China. E-mail: yongjw@bjut.edu.cn

How to cite this article: Yong J, Dong Y, Zhang Z, Feng N, Li W. Integrated control of anti-lock and regenerative braking for in-wheel-motor-driven electric vehicles. *Complex Eng Syst* 2024;4:2. <http://dx.doi.org/10.20517/ces.2023.36>

Received: 10 Oct 2023 **First Decision:** 8 Nov 2023 **Revised:** 23 Nov 2023 **Accepted:** 5 Dec 2023 **Published:** 12 Jan 2024

Academic Editor: Hamid Reza Karimi **Copy Editor:** Fangling Lan **Production Editor:** Fangling Lan

Abstract

The in-wheel motor is increasingly used in electric vehicles due to the significantly improved controllability, response capability, and energy recovery efficiency based on this technology. However, the independent control of in-wheel motors will lead to braking torque distribution problems, especially in a situation where anti-lock braking systems (ABS) are triggered, which may cause the braking energy to be unrecoverable without the coordinated control between anti-lock and RB for two in-wheel motor-driven electric vehicles based on the RB efficiency map. Control-oriented wheel dynamics and slip ratio models of the system are generated. A sliding mode intervention of regenerative braking (RB) control. This paper presents an integrated algorithm to realize the control-based ABS controller is designed to prevent the wheels from locking and to maintain the slip ratio within a desired level, and the stability and robustness of the controller to uncertainties and disturbances are discussed. Moreover, the braking strength of the driver is calculated and divided into different modes to derive a dynamic braking torque distribution to improve the energy recovery efficiency. The hardware-in-the-loop simulation results show that the recovered energy of the proposed strategy under ABS-triggered maneuver is increased by 52.9% than that of the Proportional, Integral, and Derivative controller and can effectively improve the braking performance and stability.

Keywords: Anti-lock braking system, regenerative braking, sliding mode control, energy recovery, braking torque distribution, electric vehicle



© The Author(s) 2024. **Open Access** This article is licensed under a Creative Commons Attribution 4.0 International License (<https://creativecommons.org/licenses/by/4.0/>), which permits unrestricted use, sharing, adaptation, distribution and reproduction in any medium or format, for any purpose, even commercially, as long as you give appropriate credit to the original author(s) and the source, provide a link to the Creative Commons license, and indicate if changes were made.



1. INTRODUCTION

Many studies imply that almost one-half of the driving energy is dissipated during braking, especially in urban driving circumstances with frequent acceleration and deceleration manipulations^[1,2]. The energy consumption during braking processes in different driving cycles is shown in Table 1^[3], where UDDS and ECE stand for urban dynamometer driving schedule and Economic Commission of Europe, respectively. Therefore, regenerative braking systems (RBS), which could recapture kinetic energy and greatly reduce power consumption^[5], are widely researched in electric or hybrid vehicles^[4–6], and brake-by-wire systems^[7,8] that support the application of regenerative braking (RB) are investigated as well^[7–10]. Xu *et al.* divided the braking into four different modes for hybrid electric vehicles, and a hierarchical controller is designed to switch the braking mode and to realize optimal efficiency control^[11]. Guo *et al.* presented a piecewise RB strategy for safety and energy-saving control of intelligent electric vehicles^[12]. However, the above strategies do not take the vehicle braking stability into consideration, which will cause the vehicle instability in limited conditions. Biao *et al.* proposed an optimization distribution algorithm-based RB strategy considering vehicle stability during braking situations^[13]. The torque distribution ratio is determined by the braking strength and related constraint conditions, and the energy recapture efficiency of the proposed strategy was raised by about fifty percent, but the stability effect of the vehicle was not reflected in the verification part.

The in-wheel motor, which is located directly in the wheels, will significantly enhance controllability and response speed by removing all the intermediate mechanical connections. Additionally, it acquires high efficiency both in motor and generator modes^[14]. Therefore, the control strategies for in-wheel motor-driven electric vehicles (IWMDEV) have been widely studied. Karabacak *et al.* designed a fuzzy logic controller in the motor mode and a pulse width modulation controller in the RB mode for two IWMDEV (2IWMDEV), and the algorithm is embedded in a DSP microcontroller^[15]. Gang and Zhi proposed an RB control method for four IWMDEV (4IWMDEV) under urban scenes using motor efficiency maps, and the simulation results validated the effectiveness of the proposed method under urban driving cycles^[16]. A feedback hierarchical controller for 4IWMDEV is presented by Chen *et al.* to control the vehicle to track the desired velocity and assign braking torque to increase energy recovery^[17]. However, in addition to improving recovery efficiency, the braking performance and stability should also be considered, especially under heavy braking strength request conditions, which will cause the braking torque distribution problem^[18–21].

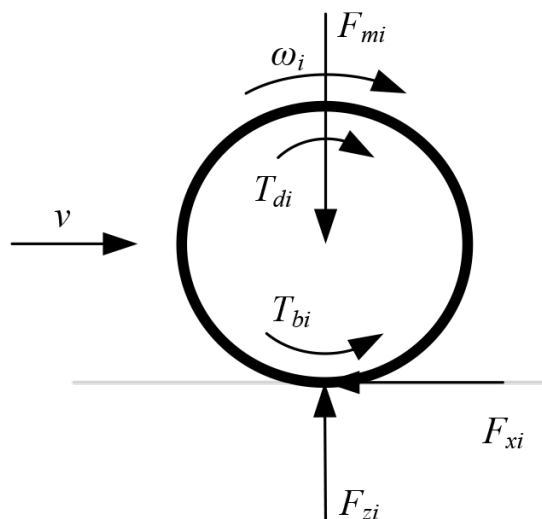
Dadashnialehi *et al.* estimated wheel speed accurately based on the back electromotive force of the brushless DC (BLDC) motor, and proposed a sensorless anti-lock braking system (ABS) for IWMDEVs both theoretically and experimentally^[22]. Wang and He presented an improved linear quadratic Gaussian controller to derive braking torques for ABS control, and a varying charge voltage in steps control is designed to recover more energy^[23]. Yang *et al.* employed a combination method of logic threshold and phase plane theory to generate the braking torque for ABS control and then proposed a coordination strategy of RBS and ABS to increase recovery efficiency for ABS-triggered scenarios^[24]. Although these methods integrate the RBS and ABS control together to improve the braking performance and recover more energy, rarely do these methods address the stability problem during braking situations. He *et al.* took the braking stability into consideration and designed a combined sliding mode controller to realize ABS control^[25]. Tang *et al.* presented a comprehensive controller: the braking torque distribution strategy. This strategy considers safety and recovery efficiency optimization while also involving a coordinated strategy of RBS and ABS based on model predictive control^[26]. Pei *et al.* proposed a coordinated controller to realize optimal energy regeneration and braking stability for distributed electric vehicles by regulating hydraulic and RB torques^[27]. However, the braking intensification is rarely considered during the coordinated control of energy recovery and braking stability.

The above studies indicate that the problem of how to simultaneously improve the braking stability and regeneration efficiency for 2IWMDEVs considering braking intensification is still not resolved. This paper aims to present an integrated control method to combine ABS and RBS control, even in emergency braking situa-

Table 1. Energy consumption during braking processes

Drive Cycle	UDDS	Japanal015	ECE
Total energy consumption, kJ	28241	1814	395
Braking energy consumption, kJ	13432	938	207
Rate, %	47.6	51.7	52.3

UDDS: Urban dynamometer driving schedule; ECE: Economic Commission of Europe.

**Figure 1.** Wheel dynamic.

tions, and synthetically improve braking performance, recovery efficiency, stability, and road adaptability of 2IWMDEVs. The main contributions of the paper include a robust SMC-based ABS controller to make full use of the road conditions under different adhesion coefficients and an RBS strategy to distribute the regenerative and hydraulic braking torques to recapture more energy.

The rest of the paper is organized as follows: In the second section, a SMC-based ABS controller is proposed for 2IWMDEVs, including wheel dynamics models, slip ratio models, ABS controllers, and stability and robustness analysis of the controller. The distribution method of regenerative and frictional braking torques is designed in the third section. In the fourth section, the RB efficiency map is generated through bench experiments. Hardware-in-the-loop (HIL) simulations are conducted in the fifth section to validate the proposed algorithm. Finally, within the same section, conclusions are made, and a future work outlook is provided.

2. SMC-BASED ABS CONTROLLER

2.1 Wheel dynamics

An electric vehicle equipped with two front in-wheel motors and RBSs is applied in the paper, and the two rear wheels are driven by a traction motor. Figure 1 shows rotational dynamics of single wheels, where T_{di} and T_{bi} represent drive and brake torques on the i -th wheel, respectively, F_{mi} , F_{xi} , and F_{zi} denote gravity, longitudinal force, and vertical force on the tire, respectively. ω_i stands for velocity of the i -th wheel, and v is vehicle velocity.

The following assumptions are made.

- The tire rolling resistance and vehicle aerodynamics are negligible during braking processes.
- Tire self-aligning torque is negligible.
- The chamber angle of each wheel is zero.

The dynamic equations are as follows.

$$m_i \dot{v} = F_{xi} \quad (1)$$

$$J_{\omega_i} \dot{\omega}_i = -T_{bi} + r F_{xi} \quad (2)$$

$$F_{xi} = \mu_i(\lambda_i) F_{zi} \quad (3)$$

where J_{ω_i} represents the rotational inertia of the i -th in-wheel motor, m_i is the total mass distributed on the i -th wheel, r is the effective wheel rolling radius, and μ_i and λ_i present longitudinal utilized friction coefficient and the slip ratio of the i -th wheel, respectively.

Combining Equations (1), (2), and (3) yields

$$\begin{cases} \dot{\omega}_i = \frac{-T_{bi} + r \mu_i(\lambda_i) F_{zi}}{J_{\omega_i}} \\ \dot{v} = \frac{-\sum \mu_i(\lambda_i) F_{zi}}{m_i} \end{cases} \quad (4)$$

where the slip ratio could be expressed as follows during braking situations

$$\lambda_i = \frac{v - r \cdot \omega_i}{v} \quad (5)$$

Taking the derivative of Equation (5) with respect to time and substituting Equation (4) into it, we have

$$\dot{\lambda}_i = \frac{r}{J_{\omega_i} v} T_{bi} - \frac{r^2}{J_{\omega_i} v} \mu_i(\lambda_i) F_{zi} - \frac{r \omega_i}{m_i v^2} \sum \mu_i(\lambda_i) F_{zi} \quad (6)$$

Figure 2 represents experimental results based on JAC iEV7S, a four-wheel double-drive electric vehicle; it shows the relationship between slip ratios and longitudinal utilized friction coefficients, and the curve could be simplified with two lines intersecting at the peak utilized friction coefficient point. The longitudinal utilized friction coefficient can be described as follows

$$\mu_i(\lambda_i) = \begin{cases} k_{\mu_{it}} \lambda_i, & \lambda_i \leq \lambda_{di} \\ \mu_{imax} - k_{\mu_{ih}} (\lambda_i - \lambda_{di}), & \lambda_i > \lambda_{di} \end{cases} \quad (7)$$

where $k_{\mu_{it}}$ and $k_{\mu_{ih}}$ denote the slope of lines corresponding to linear and nonlinear areas, respectively, λ_{di} stands for reference slip ratios for the i -th wheel, and μ_{imax} represents peak longitudinal utilized friction coefficients of the i -th wheel.

Substituting Equation (7) into Equation (6), after some manipulations, we have

$$\dot{\lambda}_i = \begin{cases} \frac{r}{J_{\omega_i} v} T_{bi} - \frac{r^2}{J_{\omega_i} v} \lambda_i k_{\mu_{it}} F_{zi} - \frac{r \omega_i}{m_i v^2} \sum k_{\mu_{it}} \lambda_i F_{zi}, & \lambda_i \leq \lambda_{di} \\ \frac{r}{J_{\omega_i} v} T_{bi} - \frac{r^2}{J_{\omega_i} v} (\mu_{imax} - k_{\mu_{ih}} (\lambda_i - \lambda_{di})) F_{zi} - \frac{r \omega_i}{m_i v^2} \sum (\mu_{imax} - k_{\mu_{ih}} (\lambda_i - \lambda_{di})) F_{zi}, & \lambda_i > \lambda_{di} \end{cases} \quad (8)$$

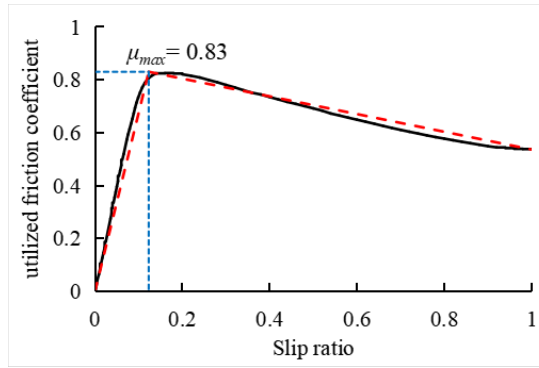


Figure 2. The curve of μ_i and λ_i .

2.2 ABS controller

ABS controllers are designed to maintain the slip ratios of wheels at a particular level, where both the longitudinal and lateral adhesion forces reach their maximum value. To this end, we define the sliding surface in terms of slip ratio tracking errors as

$$S_i = \lambda_{di} - \lambda_i \tag{9}$$

It is apparent that if we find a control law to make S_i converge to zero or maintain small, then the slip ratio will match very well with the desired one. However, a drastic change of the control law will occur when S_i is near the sliding surface. To eliminate the chattering problem and smooth the control law, for the system motion on the sliding surface, control rules are designed below.

$$\dot{S}_i = -K_i \text{sat}(S_i/\varphi) \tag{10}$$

$$\text{sat}(S_i/\varphi) = \begin{cases} S_i/\varphi, & |S_i/\varphi| \leq 1 \\ \text{sgn}(S_i/\varphi), & |S_i/\varphi| > 1 \end{cases} \tag{11}$$

where K_i is positive and denotes the factor of convergence; $\text{sat}(S/\varphi)$ stands for the switching function, and φ represents the boundary layer thickness.

Differentiating Equation (9) with respect to time and combining Equation (8) yield

$$\dot{S}_i = \begin{cases} \dot{\lambda}_{di} - \frac{r}{J_{\omega i} v} T_{bi} - \frac{r^2}{J_{\omega i} v^2} k_{\mu i t} \lambda_i F_{z i} - \frac{r \cdot w_i}{m_i v^2} \sum k_{\mu i t} \lambda_i F_{z i}, & \lambda_i \leq \lambda_{di} \\ \dot{\lambda}_{di} - \frac{r}{J_{\omega i} v} T_{bi} - \frac{r^2}{J_{\omega i} v^2} (\mu_{imax} - k_{\mu i h} (\lambda_i - \lambda_{th})) F_{z i} - \frac{r \cdot w_i}{m_i v^2} \sum (\mu_{imax} - k_{\mu i h} (\lambda_i - \lambda_{di})) F_{z i}, & \lambda_i > \lambda_{di} \end{cases} \tag{12}$$

Since λ_{di} is a constant, which means $\dot{\lambda}_{di} = 0$, substituting Equation (10) into Equation (12), the control law will be derived.

$$T_{bi} = \begin{cases} r k_{\mu it} \lambda_i F_{zi} + \frac{J \omega_i \omega_i}{m_i v} \sum k_{\mu it} \lambda_i F_{zi} + K_i \frac{J \omega_i v}{r} \operatorname{sat} \left(\frac{\lambda_{di} - \lambda_i}{\varphi} \right), & \lambda_{di} > \lambda_i \\ r (\mu_{imax} - k_{\mu ih} (\lambda_i - \lambda_{di})) F_{zi} + K_i \frac{J \omega_i v}{r} \operatorname{sat} \left(\frac{\lambda_{di} - \lambda_i}{\varphi} \right) + \frac{J \omega_i \omega_i}{m_i v} \sum (\mu_{imax} - k_{\mu ih} (\lambda_i - \lambda_{di})) F_{zi}, & \lambda_{di} > \lambda_i \end{cases} \quad (13)$$

2.3 Stability analysis of the ABS controller

The Lyapunov function is designed as follows:

$$W_i = (\lambda_{di} - \lambda_i)^2 \quad (14)$$

Thus,

$$\dot{W}_i = 2 (\lambda_{di} - \lambda_i) (\dot{\lambda}_{di} - \dot{\lambda}_i) \quad (15)$$

Substituting Equation (8) into Equation (15), after some manipulations, we have

$$\dot{W}_i = \begin{cases} -2 (\lambda_{di} - \lambda_i) \left(\frac{r}{J \omega_i v} T_{bi} - \frac{r^2}{J \omega_i v} k_{\mu it} \lambda_i F_{zi} - \frac{r \omega_i}{m_i v^2} \sum k_{\mu it} \lambda_i F_{zi} \right), & \lambda_i \leq \lambda_{di} \\ -2 (\lambda_{di} - \lambda_i) \left(\frac{r}{J \omega_i v} T_{bi} - \frac{r^2}{J \omega_i v} (\mu_{imax} - k_{\mu ih} (\lambda_i - \lambda_{di})) F_{zi} - \frac{r \omega_i}{m_i v^2} \sum (\mu_{imax} - k_{\mu ih} (\lambda_i - \lambda_{th})) F_{zi} \right), & \lambda_i > \lambda_{di} \end{cases} \quad (16)$$

Substituting Equation (13) into Equation (16) yields

$$\dot{W}_i = -2 (\lambda_{di} - \lambda_i) K_i \operatorname{sat} \left(\frac{\lambda_{di} - \lambda_i}{\varphi} \right) \leq 0 \quad (17)$$

The stability of the proposed ABS controller has been proved, and the system will move to the surface according to Equation (17). Assume that the initial slip ratio tracking error is finite, and then, S_i will arrive at the sliding surface $S_i=0$ in a finite time.

2.4 Robustness analysis of the ABS controller

Nonlinear characteristics, disturbances, and uncertainties always exist in practice control systems, e.g., motor torques, estimated vehicle velocity, and sensor noise. Therefore, if the controller is to be applied in practice, it is essential to analyze its robustness.

2.4.1 Disturbance analysis of motor torque

In the actual motor control process, it is generally difficult to achieve real-time precise implementation of the desired motor torque listed in Equation (13), and the torque tracking error may reduce the control performance or even cause the controller instability. Moreover, the additive disturbance will affect the design value of convergence factor K_i . Therefore, the desired motor torque is redesigned with a torque disturbance item added in Equation (13) as

$$T_{bia} = T_{bi} + \Delta T_{bi} \quad (18)$$

Replacing T_{bi} with T_{bia} in Equation (16) and combining Equation (13), we have

$$\dot{W}_i = -2 (\lambda_{di} - \lambda_i) \left[\frac{r}{J_{wi}v} \Delta T_{bi} + K_i \operatorname{sat} \left(\frac{\lambda_{di} - \lambda_i}{\varphi} \right) \right] \quad (19)$$

Note that the first derivative of the Lyapunov function should be negative definite to ensure the system stability; the torque disturbance should satisfy the following inequality constraints.

$$|\Delta T_{bi}| \leq \left| K_i \frac{J_{wi}v}{r} \operatorname{sat} \left(\frac{\lambda_{di} - \lambda_i}{\varphi} \right) \right| \quad (20)$$

The above equation means that the factor of convergence K_i should be large enough to cover the disturbance caused by the control error, and then the stability of the controller will be guaranteed.

2.4.2 Disturbance analysis of vehicle velocity

The actual vehicle velocity is normally obtained from the transmission output shaft speed sensor or estimated based on the wheel speed sensor. However, the above methods will cause velocity error, which leads to slip ratio error $\Delta\lambda_i$, and with Equation (5), we have

$$\Delta\lambda_i = \frac{v + \Delta v - v_{wi}}{v + \Delta v} - \frac{v - v_{wi}}{v} \approx \frac{\Delta v}{v} \quad (21)$$

For the controller, the actual slip ratio is expressed as $\lambda_i + \Delta\lambda_i$, considering torque disturbance, Equation (17) is updated.

$$\dot{W}_i = -2 (\lambda_{th} - \lambda_i - \Delta\lambda_i) K_i \operatorname{sat} \left(\frac{\lambda_{th} - \lambda_i - \Delta\lambda_i}{\varphi} \right) \leq 0 \quad (22)$$

From the above equation, \dot{W}_i will always be negative definite no matter if the velocity error is large or small, which implies that the controller has strong robustness under velocity disturbance.

2.4.3 Disturbance analysis of sensor noise

Sensor noise has a significant influence on the stability of a closed-loop system, and the signal fluctuation will degrade measurement accuracy and affect state parameter calculation; e.g., the fluctuation of wheel velocity signals will influence the slip ratio calculation according to Equation (5). High-frequency filters^[7] are adopted to estimate the actual value, decrease measurement noise, and guarantee the system stability.

3. DISTRIBUTION OF REGENERATIVE AND FRICTIONAL BRAKING TORQUES

With two front in-wheel motors, the regenerative and frictional blending brake is related, and the optimal objective is to improve energy recovery efficiency and braking stability. To this end, the distribution of the regenerative and frictional braking torques should be first discussed. As shown in Figure 3, the requested braking pressure of the driver is calculated according to brake pedal stroke and the characteristics of brake pressure *vs.* pedal stroke (P-S curve) shown in reference^[7], and then the requested braking force F_b and torque T_b are estimated. A braking torque distribution controller is designed to generate the desired regenerative and frictional braking torques according to the braking strength. The RB torque is executed by the in-wheel motors,

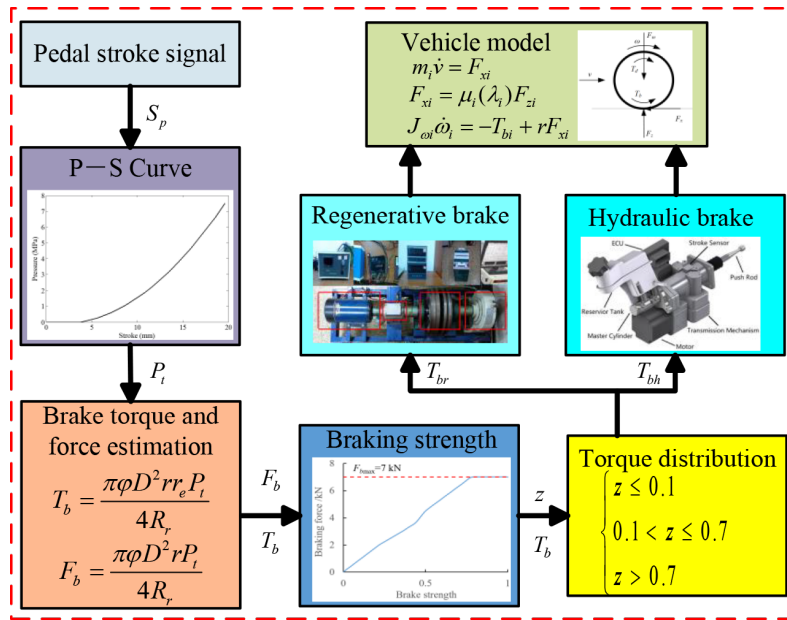


Figure 3. Braking torque control schematic.

while the frictional braking torque is realized by a novel electro-hydraulic actuator illustrated in reference [28], and the novel electro-hydraulic actuator generates braking force fast and has a fast and good pressure-tracking performance.

To improve tire-road friction coefficient (TRFC) utilization efficiency and directional stability during braking situations, both the front and rear wheels should be locked simultaneously, and the desired braking forces of the front and rear axles are expressed as follows

$$\begin{cases} F_{\mu 1} + F_{\mu 2} = F_b \\ F_{\mu 2} = \frac{1}{2} \left[\frac{G}{h_g} \sqrt{b^2 + \frac{4h_g L}{G} F_{\mu 1}} - \left(\frac{Gb}{h_g} + 2F_{\mu 1} \right) \right] \end{cases} \quad (23)$$

where $F_{\mu 1}$ and $F_{\mu 2}$ denote the desired braking forces of the front and rear axles, respectively, G stands for the weight of vehicles, L represents wheelbase, b is the horizontal distance between the rear axle and center of gravity, and h_g indicates the height of the center of gravity with respect to the ground.

With manipulations of Equation (23), we have

$$\begin{cases} F_{\mu 1} = \frac{F_b^2 h_g + F_b G b}{GL} \\ F_{\mu 2} = F_b - F_{\mu 1} \end{cases} \quad (24)$$

As shown in Figure 3, the braking strength z is achieved according to the requested braking force and F_b - z lookup table. The braking mode is divided into three levels: mild ($z \leq 0.1$), moderate ($0.1 < z \leq 0.7$), and emergency ($z > 0.7$), and the braking torque distribution strategy is discussed based on different modes.

(A) When $z \leq 0.1$, the requested braking torque of the front axle will be offered only by the two front regenerative motors; the braking torque distribution of axles and blended braking system are derived

$$\begin{cases} T_{bfr} = F_{\mu 1}r, T_{bfh} = 0 \\ T_{br} = F_{\mu 2}r \end{cases} \quad (25)$$

where T_{bfr} and T_{bfh} represent regenerative and hydraulic braking torques of the front axle, respectively, and the braking torque of the left and right wheels of the front axle is allocated averagely; T_{br} denotes the braking torque of the rear axle.

(B) When $0.1 < z \leq 0.7$, the RB torque may not meet the request one, and the braking torques are distributed as follows

$$\begin{cases} T_{bfr} = F_{\mu 1}r, T_{bfh} = 0, T_{br} = F_{\mu 2}r; & T_{bf} \leq T_{bfr \max} \\ T_{bfr} = T_{bfr \max}, T_{bfh} = T_{bf} - T_{bfr \max}, T_{br} = F_{\mu 2}r; & T_{bf} > T_{bfr \max} \end{cases} \quad (26)$$

where $T_{bf} = (F_b^2 h_g + F_b G b)r / GL$ is the braking torque calculated by Equation (24), $T_{bfr \max}$ stands for the maximum RB torque that both the left and right motors could be applied for at the same time.

(C) When $z > 0.7$, the braking torque distribution is the same as Equation (26) if the wheels are not locked. However, the ABS will probably be triggered in this large deceleration request situation, and the braking torques of the front and rear axles will not be decided by Equation (24) but rather by the results generated from ABS controllers. In this case, the torque distribution is determined by

$$\begin{cases} T_{bfff} = T_{bffA}, T_{bfih} = 0, T_{bri} = T_{briA}; & T_{bffA} \leq T_{bfr \max} \\ T_{bfff} = T_{bfr \max}, T_{bfih} = T_{bffA} - T_{bfr \max}, T_{bri} = T_{briA}; & T_{bffA} > T_{bfr \max} \end{cases} \quad (27)$$

where T_{bffA} and T_{briA} stand for desired braking torques of the four wheels generated by the ABS controller, T_{bfff} and T_{bfih} represent distributed regenerative and hydraulic braking torques of the front two wheels, and T_{bri} is braking torque of two rear wheels.

4. EFFICIENCY MAP OF THE RB SYSTEM

An optimal energy recovery method should be designed based on an efficiency map by minimizing the transfer loss during blending brake, and the motor-to-battery efficiency is calculated by the following expression.

$$\eta = \frac{U_C I_C}{T_b \omega} \quad (28)$$

where U_C and I_C are the measured battery charging voltage and current during RB, respectively.

Figure 4 shows the test bench; a motor with the same characteristics is used instead of the in-wheel one, and a magnetic powder brake is adopted to simulate the vehicle rolling resistance to prevent the motor from moving or to supply kinetic energy during braking. Batteries and sensors are installed to collect energy recapture information. With Equation (28), the RB efficiency map is generated from bench tests under different braking torques and wheel velocities and is fitted, as shown in Figure 5, based on the experimental data.

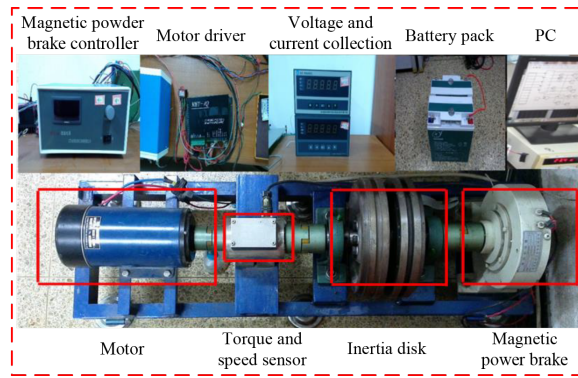


Figure 4. Test bench.

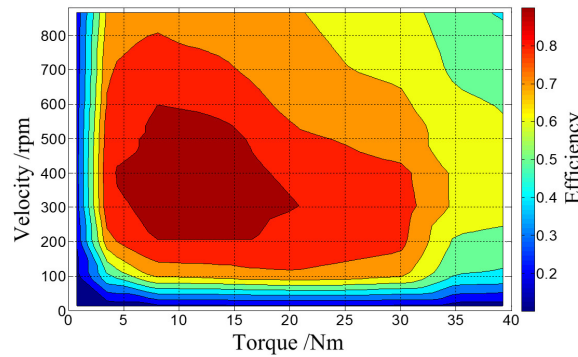


Figure 5. RB efficiency map.

Table 2. Vehicle model and controller parameters

Parameters	Value
Vehicle mass (m)	1,855 kg
Rotational inertia of the front/rear tire (J_{wt})	1.5 kg·m ²
Effective wheel rolling radius (r)	316 mm
Height of the center of gravity (h_g)	530 mm
Distance between the front and rear axles (L)	2,490 mm
Front axle to the center of gravity (a)	1,100 mm
Rear axle to the center of gravity (b)	1,390 mm
Effective radius of the front brake disc (r_b)	105 mm
Piston radius of the front wheel cylinder (r_w)	27 mm
Friction coefficient of the front brake pad (μ_f)	0.4
Maximum RB torque (T_{hfrmax})	1,200 N
Convergence factor (K_f)	0.02
Boundary layer thickness (ϕ)	0.1

5. HIL SIMULATION AND RESULTS ANALYSIS

A HIL simulation system equipped with vehicle-manipulator systems, steering systems, and hydraulic braking system is developed to evaluate the performance of the proposed integrated algorithm. Figure 6 displays the system composition. Figure 7 illustrates the algorithm block diagram. In this diagram, the steering angle and braking torque are requested by the driver. The vehicle model is then simulated using the CarSim software. The torque distribution and ABS algorithm code are generated using MATLAB/Simulink and downloaded to the dSPACE/SCALEXIO for execution. Finally, the recaptured energy is stored in the battery pack. The vehicle model and controller parameters are listed in Table 2.

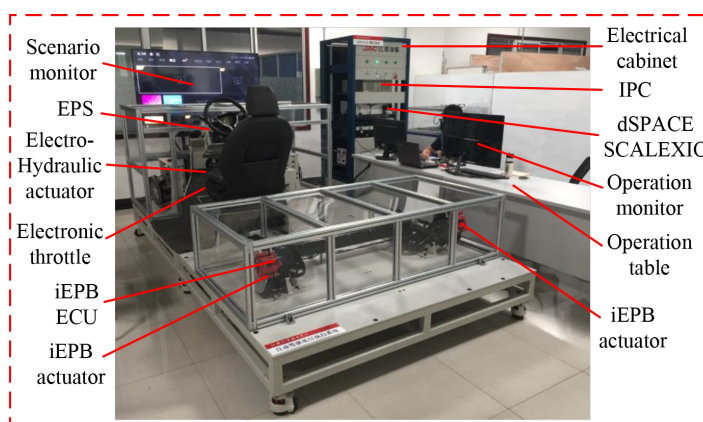


Figure 6. HIL simulation system.

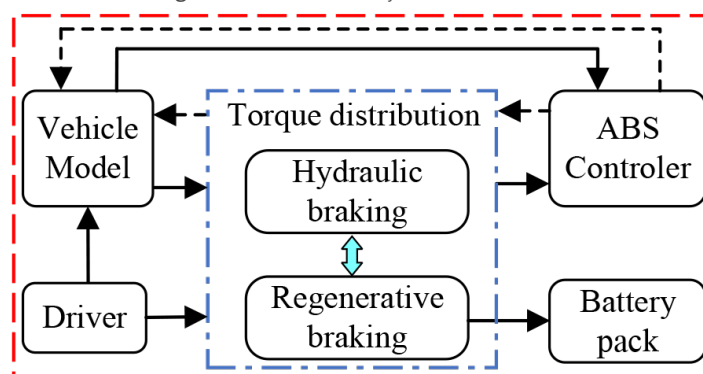


Figure 7. Algorithm block diagram.

5.1 Results on homogeneous surface

A steering-braking maneuver with a 75 km/h initial forward velocity is performed on a high- μ homogeneous surface to verify the proposed algorithm, and a Proportional, Integral, and Derivative (PID) controller is also simulated to compare with the proposed one. Figure 8 shows the time histories of vehicle and wheel velocities derived from the two controllers under the specified simulation maneuver. At the end of the simulation, the four wheels of the PID controller are locked, while those of the SMC controller are not during the whole simulation, which indicates that the proposed SMC controller achieves better anti-lock performance than the PID controller. As shown in Figure 8A and B, compared with PID controllers, the regulation frequency of the front wheels of SMC controllers is lower, which will improve the vehicle stability and comfort.

Figure 9 depicts the comparison of wheel slip ratios derived from the two controllers. Slip ratios of all the wheels of both the controllers are within a reasonable range near the optimal value in the beginning, and then, the fluctuation of the PID controller dramatically rises to approximately one while that of the SMC controller is still reasonable. The high braking torque regulation frequency of front wheels leads to frequent and dramatic chattering of the slip ratio. The results illustrate that the SMC controller acquires a significantly better tracking performance of the optimal slip ratio.

Figure 10 presents the time histories of sideslip angular velocities and yaw rates. In Figure 10A, although the fluctuations of both two controllers are large in the beginning because of the steering input, the sideslip angular velocity derived from the SMC controller is constrained within a very small boundary in the remaining simulation process, while that of the PID method is still variate intensive. As shown in Figure 10B, the magnitude of the yaw rate of the PID controller is much larger than that of the SMC controller, especially at the

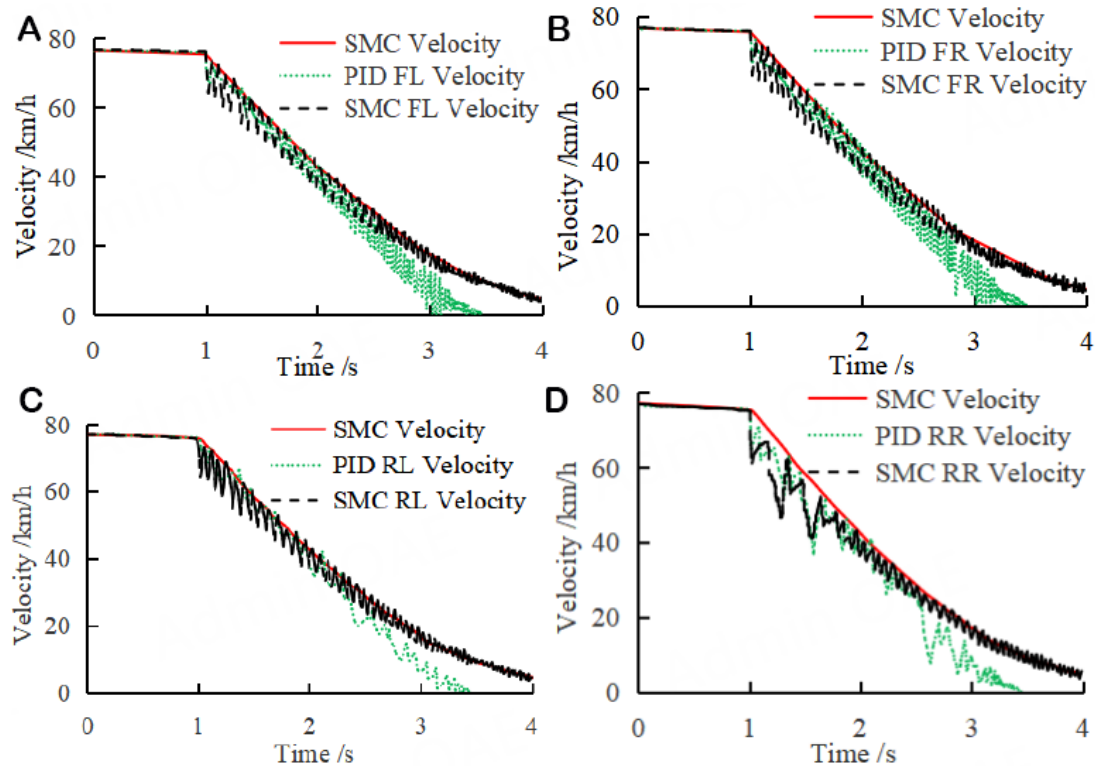


Figure 8. Velocities of vehicles and wheels. (A) Front left wheel; (B) Front right wheel; (C) Rear left wheel; (D) Rear right wheel.

end of the simulation. The results indicate that the proposed method achieves a better handling and stability performance than that of the PID controller.

Figure 11 and Figure 12 reveal the comparison of energy recovery between the SMC and PID controllers. Since the braking torque generated by the SMC controller is much bigger than that of the PID controller before about 1.5 s, the recapture energy of the SMC controller is larger during the beginning period. After about 2.4 s, the braking torque derived from PID is larger than SMC, which causes a greater wheel velocity variation even to lock, as shown in Figure 8. However, the recaptured energy by SMC grows faster than by PID due to the distribution of braking torques, and the main growth of recovery energy by SMC lies in this period. Overall, the SMC-based energy recovery efficiency is significantly higher than that of PID-based, and the efficiency increases by 52.9%.

5.2 Results on the split surface

A driver-in-the-loop simulation on the split surface with a 70 km/h initial forward velocity is conducted to evaluate the effectiveness of the proposed algorithm in non-ideal scenarios, and the TRFCs of the left and right sides are 0.3 and 0.8, respectively. Figure 13A shows the master cylinder pressure applied by the driver and the wheel cylinder pressures generated by the ABS controller. The applied pressure (about 8 MPa) is too big to anti-lock the wheels, and the ABS is triggered to regulate the wheel pressures. Furthermore, the generated pressures of the left wheels change more frequently than the right wheels due to the lower TRFC, and the pressure increasement times of the front left (FL) and rear left (RL) wheels are 25 and 26 in approximately eight seconds, whereas that of the front right (FR) and rear right (RR) are two and 24 times, respectively. Although the left wheels are easier to lock up due to their huge fluctuations of slip ratios, the frequent regulation of braking pressures keeps the wheels in anti-lock status, as shown in Figure 13B. The maximum equivalent braking pressure generated by the RB motor is calculated by the following expression.

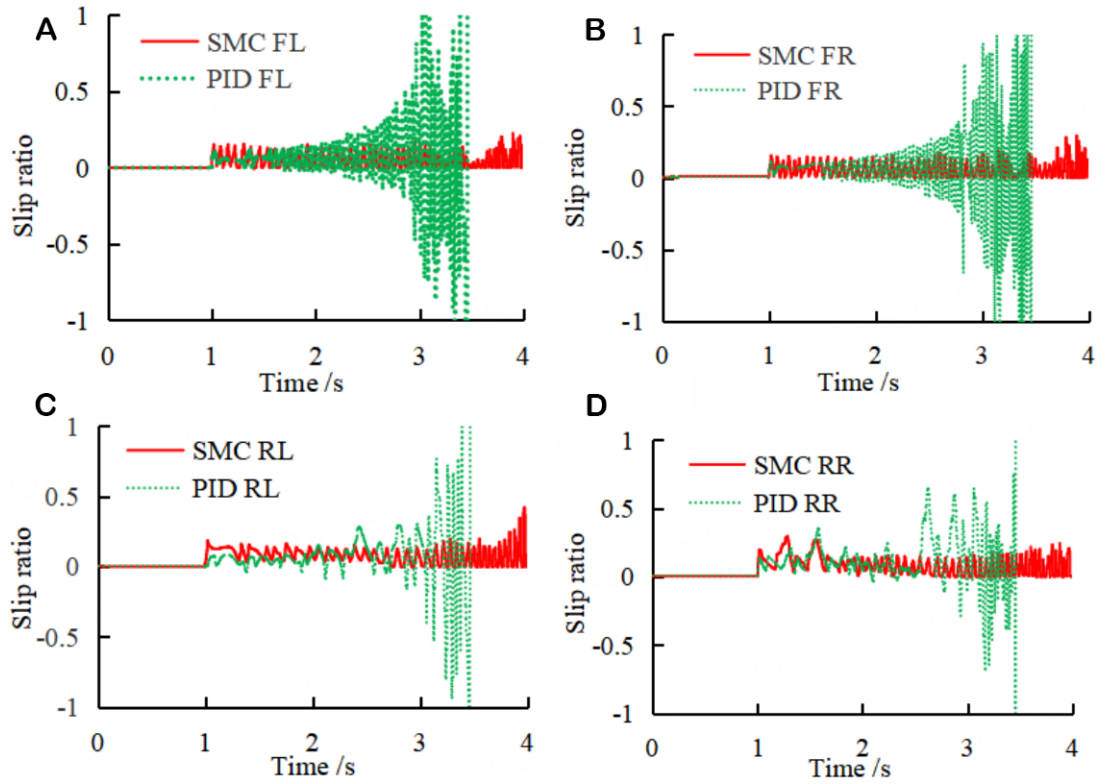


Figure 9. Slip ratio of the wheels.(A) Front left wheel; (B) Front right wheel; (C) Rear left wheel; (D) Rear right wheel.

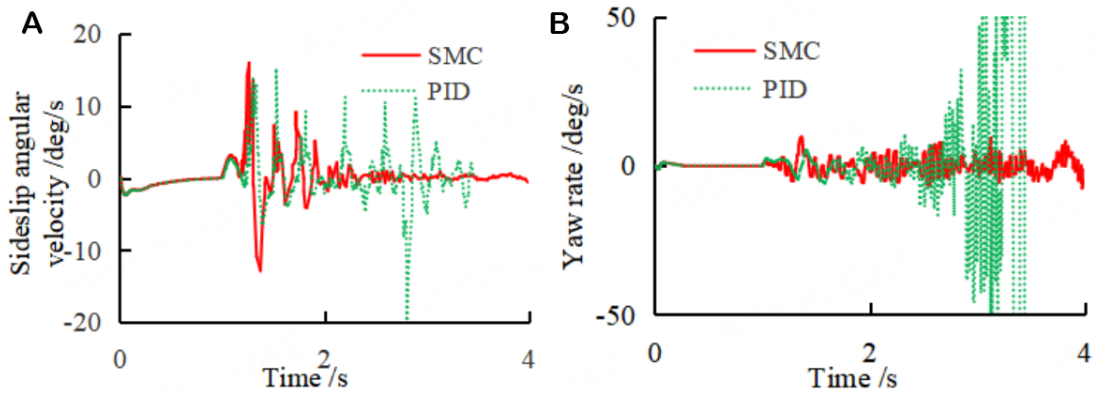


Figure 10. Vehicle sideslip angular velocity and yaw rate. (A) Sideslip angular velocity; (B) Yaw rate.

$$P_{mr} = \frac{F_{bfr} \max r}{2\pi r_w^2 \mu r_b} \tag{29}$$

With the parameter values listed in Table 2, the value of P_{mr} is calculated as 2 MPa. Figure 13C and D indicates the braking distribution results of the front wheels derived from the proposed algorithm; only RB is applied if the pressure generated by the ABS controller is less than 2 MPa, and the residual pressure is generated by the hydraulic braking system.

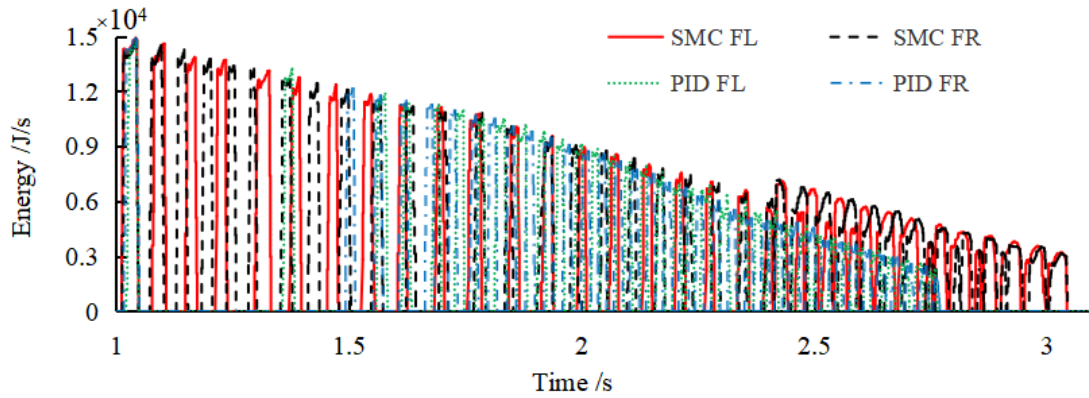


Figure 11. Distribution of the regenerative braking energy.

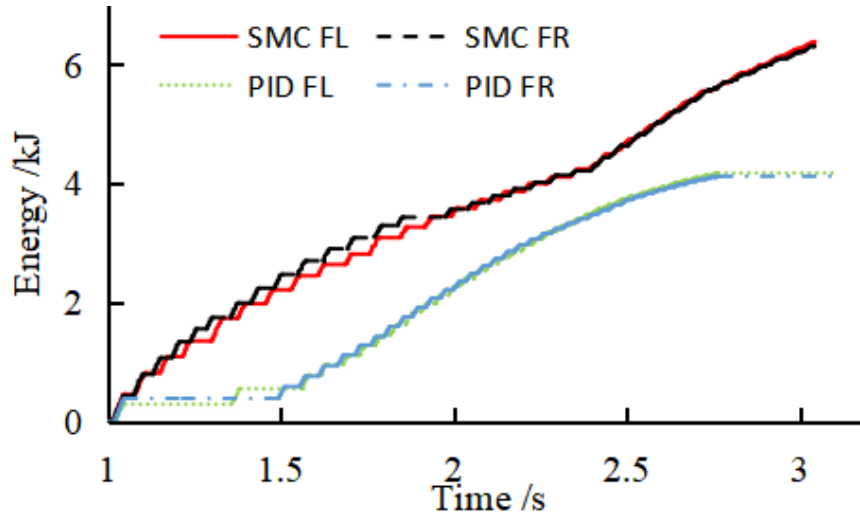


Figure 12. Comparison of total recaptured energy.

6. CONCLUSIONS AND FUTURE WORK

An integrated algorithm is proposed for ABS and RBS coordinated control of 2IWMDEVs to improve vehicle braking stability and energy recovery efficiency, including both RB control on the front two wheels and anti-lock braking control on all four wheels. HIL simulations are carried out to verify the effectiveness of the integrated algorithm, and the results show that the ABS controller can prevent wheels from being locked to ensure braking performance and vehicle stability. With the distribution strategy of braking torques among in-wheel motors and friction brakes considering the required braking torque and strength, the recovered energy of the proposed strategy under ABS-triggered maneuver is increased by 52.9% than that of the PID controller. Therefore, the presented integrated algorithm can not only maintain the slip ratio within the desired range and braking stability but also achieve excellent energy recapture efficiency, which is significant to ensure safety and economy of the 2IWMDEVs.

Our future work will concentrate on adaptive threshold value design for braking modes division, experimental validation of the proposed algorithm through in-vehicle field and road tests with the consideration of uncertainties, and modification of the proposed algorithm to adapt to 4IWMDEVs.

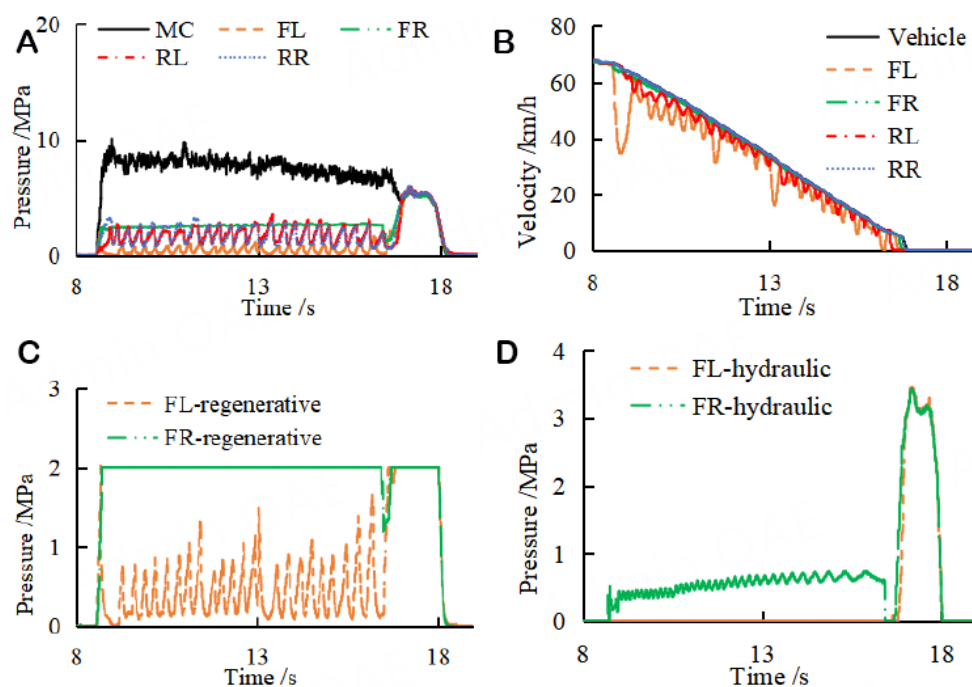


Figure 13. Simulation results on the split surface. (A) Braking pressure; (B) Velocities; (C) Regenerative braking; (D) Hydraulic braking.

DECLARATIONS

Acknowledgments

The authors would like to thank the anonymous reviewers for their valuable comments.

Authors' contributions

Made substantial contributions to the conception and design of the study and performed data analysis and interpretation: Yong J, Dong Y, Zhang Z

Performed data acquisition and provided administrative, technical, and material support: Zhang Z, Feng N, Li W

Availability of data and materials

Not applicable.

Financial support and sponsorship

This work was supported by the National Natural Science Foundation of China (No. 52002009), Beijing Natural Science Foundation (No. 3222003), and the State Key Laboratory of Automotive Safety and Energy under Project No. KF2010.

Conflicts of interest

All authors declared that there are no conflicts of interest.

Ethical approval and consent to participate

Not applicable.

Consent for publication

All the authors have agreed to publish the paper.

Copyright

© The Author(s) 2024.

REFERENCES

1. Feng N, Yong J, Zhan Z. A direct multiple shooting method to improve vehicle handling and stability for four hub-wheel-drive electric vehicle during regenerative braking. *J Automot Eng* 2019;234:1047-56. DOI
2. Zhao W, Wu G, Wang C, Yu L, Li Y. Energy transfer and utilization efficiency of regenerative braking with hybrid energy storage system. *J Power Sources* 2019;427:174-83. DOI
3. Bravo RRS, De Negri VJ, Oliveira AAM. Design and analysis of a parallel hydraulic-pneumatic regenerative braking system for heavy-duty hybrid vehicles. *Appl Energy* 2018;225:60-7. DOI
4. Xu M, Peng J, Ren X, Yang X, Hu Y. Research on braking energy regeneration for hybrid electric vehicles. *Machines* 2023;11:347. DOI
5. Choo KM, Won CY. Design and analysis of electrical braking torque limit trajectory for regenerative braking in electric vehicles with PMSM drive systems. *IEEE Trans Power Electron* 2020;35:13308-21. DOI
6. Hamada AT, Orhan MF. An overview of regenerative braking systems. *J Energy Stor* 2022;52:105033 DOI
7. Yong J, Gao F, Ding N, He Y. Design and validation of an electro-hydraulic brake system using hardware-in-the-loop real-time simulation. *Int J Automot Technol* 2017;18:603-12. DOI
8. Han W, Xiong L, Yu Z. A novel pressure control strategy of an electro-hydraulic brake system via fusion of control signals. *J Automot Eng* 2019;233:3342-57. DOI
9. Chen Q, Lv Z, Tong H, Xiong Z. Clamping force control strategy of electro-mechanical brake system using VUF-PID controller. *Actuators* 2023;12:272. DOI
10. Wang Z, Ding X, Zhang L. Chassis coordinated control for full X-by-wire four-wheel-independent-drive electric vehicles. *IEEE Trans Veh Technol* 2023;72:4394-410. DOI
11. Xu Q, Wang F, Zhang X, Cui S. Research on the efficiency optimization control of the regenerative braking system of hybrid electrical vehicle based on electrical variable transmission. *IEEE Access* 2019;7:116823-34. DOI
12. Guo J, Li W, Wang J, Luo Y, Li K. Safe and energy-efficient car-following control strategy for intelligent electric vehicles considering regenerative braking. *IEEE Trans Intell Transport Syst* 2022;23:7070-81. DOI
13. Biao J, Xiangwen Z, Yangxiong W, Wenchao H. Regenerative braking control strategy of electric vehicles based on braking stability requirements. *Int J Automot Technol* 2021;22:465-73. DOI
14. Hosseini Salari A, Mirzaeinejad H, Fooladi Mahani M. A new control algorithm of regenerative braking management for energy efficiency and safety enhancement of electric vehicles. *Energy Convers Manag* 2023;276:116564. DOI
15. Karabacak Y, Uysal A. An embedded controller application with regenerative braking for the electric vehicle. *Elektron ElektroTech* 2020;26:10-17. DOI
16. Gang L, Zhi Y. Energy saving control based on motor efficiency map for electric vehicles with four-wheel independently driven in-wheel motors. *Adv Mech Eng* 2018;10:1-18. DOI
17. Chen J, Yu J, Zhang K, Ma Y. Control of regenerative braking systems for four-wheel-independently-actuated electric vehicles. *Mechanics* 2018;50:394-401. DOI
18. Lupberger S, Degel W, Odenthal D, Bajcinca N. Nonlinear control design for regenerative and hybrid antilock braking in electric vehicles. *IEEE Trans Contr Syst Technol* 2022;30:1375-89. DOI
19. Ma Z, Sun D. Energy recovery strategy based on ideal braking force distribution for regenerative braking system of a four-wheel drive electric vehicle. *IEEE Access* 2020;8:136234-42. DOI
20. Zhang Z, Ma R, Wang L, Zhang J. Novel PMSM control for anti-lock braking considering transmission properties of the electric vehicle. *IEEE Trans Veh Technol* 2018;67:10378-86. DOI
21. Chen Y, Chen S, Zhao Y, Gao Z, Li C. Optimized handling stability control strategy for a four in-wheel motor independent-drive electric vehicle. *IEEE Access* 2019;7:17017-32. DOI
22. Dadashnialehi A, Bab-hadiashar A, Cao Z, Kapoor A. Intelligent sensorless antilock braking system for brushless in-wheel electric vehicles. *IEEE Trans Ind Electron* 2015;62:1629-38. DOI
23. Wang J, He R. Varying charge voltage in the steps control method of ABS for in-wheel motors driven electric vehicles based on an improved LQG scheme. *IEEE Access* 2018;6:15039-50. DOI
24. Yang Y, Tang Q, Bolin L, Fu C. Dynamic coordinated control of regenerative braking system and anti-lock braking system for electrified vehicles under emergency braking conditions. *IEEE Access* 2020;8:172664-77. DOI
25. He L, Ye W, He Z, Song K, Shi Q. A combining sliding mode control approach for electric motor anti-lock braking system of battery electric vehicle. *Control Eng Pract* 2020;102:104520. DOI
26. Tang Q, Yang Y, Luo C, Yang Z, Fu C. A novel electro-hydraulic compound braking system coordinated control strategy for a four-wheel-drive pure electric driven by dual motors. *Energy* 2022;241:122750. DOI
27. Pei X, Pan H, Chen Z, Guo X, Yang B. Coordinated control strategy of electro-hydraulic braking for energy regeneration. *Control Eng Pract* 2020;96:10434. DOI
28. Yong JW, Gao F, Ding NG, He YP. Pressure-tracking control of a novel electro-hydraulic braking system considering friction compensation. *J Cent South Univ* 2017;24:1909-21. DOI